Observations of Multiple Internal Wave Packets in a Tidal River Plume

Rijnsburger, Sabine; Flores, Raúl P.; Pietrzak, Julie D.; Lamb, Kevin G.; Jones, Nicole L.; Horner-Devine, Alexander R.; Souza, Alejandro J.

DOI
10.1029/2020JC016575

Publication date
2021

Document Version
Final published version

Published in
Journal of Geophysical Research: Oceans

Citation (APA)
Rijnsburger, S., Flores, R. P., Pietrzak, J. D., Lamb, K. G., Jones, N. L., Horner-Devine, A. R., & Souza, A. J. (2021). Observations of Multiple Internal Wave Packets in a Tidal River Plume. *Journal of Geophysical Research: Oceans*, *126*(8), Article e2020JC016575. https://doi.org/10.1029/2020JC016575

JGR Oceans

RESEARCH ARTICLE
10.1029/2020JC016575

Observations of Multiple Internal Wave Packets in a Tidal River Plume

Sabine Rijnsburger[1], Raúl P. Flores[2,3], Julie D. Pietrzak[1], Kevin G. Lamb[4], Nicole L. Jones[5], Alexander R. Horner-Devine[2], and Alejandro J. Souza[6]

[1]Department of Hydraulic Engineering, Delft University of Technology, Delft, Netherlands, [2]Department of Civil and Environmental Engineering, University of Washington, Seattle, WA, USA, [3]Departamento de Obras Civiles, Universidad Técnica Federico Santa María, Valparaíso, Chile, [4]Applied Mathematics, University of Waterloo, Waterloo, ON, Canada, [5]Oceans Graduate School and the Ocean Institute, University of Western Australia, Perth, WA, Australia, [6]CINVESTAV, Mérida, Mexico

Key Points:

- Internal solitary waves (ISWs) are observed in the Rhine River plume
- Multiple ISW packets are observed due to multiple tidal plume fronts
- Trapped older fronts can re-strengthen and again transition such that ISWs are released

Correspondence to:
S. Rijnsburger,
s.rijnsburger@tudelft.nl

Citation:
Rijnsburger, S., Flores, R. P., Pietrzak, J. D., Lamb, K. G., Jones, N. L., Horner-Devine, A. R., & Souza, A. J. (2021). Observations of multiple internal wave packets in a tidal river plume. *Journal of Geophysical Research: Oceans*, *126*, e2020JC016575. https://doi.org/10.1029/2020JC016575

Received 2 JUL 2020
Accepted 1 JUL 2021

Abstract Remotely sensed images document the occurrence of multiple packets of internal solitary waves (ISWs) in the Rhine River plume at the same time. We use a combination of field observations, and non-hydrostatic and hydrostatic modeling to understand the processes that lead to the generation and retention of multiple ISW packets within the Rhine plume. Previous numerical modeling shows that the tidal plume front is trapped in the mid-field plume for more than one tidal cycle due to tidal straining and recirculation within the plume, resulting in the presence of multiple fronts in the near-and mid-field plume regions. In this work, we show how variations in the strength of these fronts can lead to the release of ISW packets. We conclude that the retention of the fronts in the mid-field region of the plume and modulation in the strength of the fronts can explain the presence of multiple ISW packets. A frontal Froude number analysis shows that fronts generated during the previous ebb tide can release ISWs in addition to the newly released tidal plume front.

Plain Language Summary Rivers release large amounts of freshwater into the coastal ocean forming a river plume. Each ebb tide a tidal plume front is formed within the river plume. A front relates to large horizontal density differences, separating river and sea water. Some studies have shown that these fronts can release internal waves, which are waves that propagate horizontally between different layers of density. These waves are an important mechanism of transporting and mixing the river water further into the ocean. In this study, we observed multiple internal wave packets propagating ahead of the Rhine River tidal plume front. Our results showed that multiple tidal plume fronts were kept within the river plume by the tidal currents, generating a multi-frontal system. Both the current and previously released tidal plume fronts release internal waves, explaining the multiple internal wave packets. This is the first known observation of the release of internal waves by a front generated on a previous tidal cycle.

1. Introduction

Internal solitary waves (ISWs) are nonlinear-dispersive waves that propagate in stratified waters (Ostrovsky & Stepanyants, 1989), which support vertical and horizontal transport of nutrients, phytoplankton, and fine sediment (Bogucki et al., 1997; Da Silva et al., 2002; Klymak & Moum, 2003; Sandstrom & Elliott, 1984). Several different ISW generation mechanisms have been observed; the most common being the nonlinear-dispersive evolution of internal waves generated by the tidal flow of stratified fluid over topography (Farmer & Armi, 1999; Maxworthy, 1979; Pietrzak et al., 1990). More recently, some novel ISW generation mechanisms have been observed, including generation by river plumes (Li & Pawlowicz, 2018; Nash & Moum, 2005; Osadchiev, 2018), intrusion fronts (Bourgault et al., 2016), and bottom gravity currents (Xie et al., 2017).

At a river mouth, the release of freshwater on every ebb tide results in a pulsed discharge forming tidal plumes bounded by distinct tidal plume fronts, which are sharp transitions in density formed by convergence with the ambient water (Garvine & Monk, 1974). Tidal plume fronts are important in the near-field plume because they interact strongly with the ambient water, influencing vertical mixing and changing local water properties (Garvine & Monk, 1974; Jay et al., 2009; Kilcher & Nash, 2010; Luketina & Imberger, 1987). Hetland (2005) showed the importance of the processes in the near-field plume for the downstream

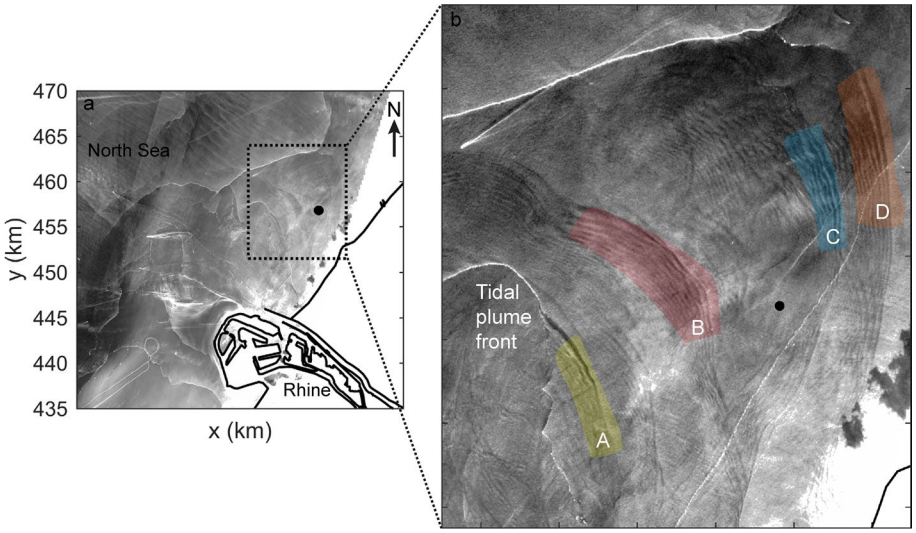

Figure 1. Copernicus Sentinel-2 optical image with a spatial resolution of 10–60 m. (a) Satellite image of the south-eastern North Sea in the vicinity of the Rhine River mouth taken on May 4, 2016 during neap tide with wind speeds < 5 m/s coming from the south. The black dot indicates the mooring site at 18 m depth. (b) inset of the internal solitary wave (ISW) bands shown by the dotted box in panel (a). Four ISW trains are highlighted by color and letter. The satellite image is Copernicus Sentinel-2 data.

evolution of river plumes. Nash and Moum (2005) observed the generation and fission of ISWs from the Columbia River plume after the front speed (u_f) transitioned from super to subcritical relative to the ambient long wave speed (c_a;$u_f < c_a$). This process was corroborated by numerical modeling (Stashchuk & Vlasenko, 2009). Similar results for gravity currents with linear background stratification were observed in laboratory experiments (Maxworthy et al., 2002).

Pan and Jay (2009a) found that front-generated ISWs impact plume dynamics by dissipating as much as 70% of the total frontal energy. Furthermore, the generation of ISWs at tidal plume fronts has a profound impact on coastal ecosystems (Hickey et al., 2010; Orton & Jay, 2005; Pan & Jay, 2009a). Despite their importance, knowledge of tidal plume front generated ISWs is limited, particularly in shallow systems where ISWs can generate large near bed velocities and bed shear stresses, which may result in sediment mobilization and resuspension (Aghsaee & Boegman, 2015).

The Copernicus Sentinel-2 optical image in Figure 1 documents the presence of the tidal plume front within the near- and mid-field regions of the Rhine River plume. Remarkably this satellite image shows four ISW packets within the mid-field plume (Figure 1 inset). This contrasts with other systems such as the Columbia River plume in which only one band of ISWs is typically observed (Jay et al., 2009; Nash & Moum, 2005; Pan et al., 2007, 2009). In the Columbia River plume and other similar systems, the ISWs are generated by the tidal plume front; they propagate away from the river mouth and generally escape the near-field plume region on each tide.

The Rhine River plume or region of freshwater influence (ROFI) is a shallow, tide-dominated system. The Rhine River flows into the southern North Sea with a yearly mean discharge of about 2,300 m^3/s forming a 20–40 km wide river plume that extends 100 km along the Dutch coast (de Kok, 1996; de Ruijter et al., 1992; Simpson et al., 1993). This coastal area is shallow with maximum water depths of about 25–30 m. The combination of a progressive tide, a shallow shelf, and stratification result in a highly frictional system, which is dominated by counter-rotating tidal currents that generate cross-shore tidal straining (de Boer et al., 2008; Simpson & Souza, 1995).

The strength of tidal straining in coastal systems is quantified by the Stokes number (Stk), which estimates the relative importance of friction and inertia in a tidal flow (Baumert & Radach, 1992; Burchard & Hetland, 2010; Prandle, 1982; Souza, 2013; Winant, 2007) and is defined as $Stk = \frac{\delta}{h}$, the ratio of the bottom

boundary layer height δ to the water depth h. The mechanisms associated with cross-shore tidal straining and the relationship to Stk are discussed in detail in Flores et al. 2020. Tidal straining is a defining dynamical feature of the Rhine plume. It generates strong shear and mixing, impacts the ecosystem, and influences patterns in coastal turbidity (Flores et al., 2020; Huthnance, 1997; Joordens et al., 2001).

Distinct tidal plume fronts have been observed to form at the Rhine River mouth (Hessner et al., 2001; van Alphen et al., 1988). An analysis of data from an extensive field campaign (Rijnsburger et al., 2018) showed that these fronts share similarities with gravity currents and other tidal plume fronts (Benjamin, 1968; Britter & Simpson, 1978; Garvine & Monk, 1974; Kilcher & Nash, 2010; Luketina & Imberger, 1987), such as a plunging head and intrinsic frontal speed. Model predictions find that turbulence is elevated at the tidal plume front (Fischer et al., 2009), which then influences coastal mixing and transport. Rhine plume fronts have been shown to propagate toward the coast, increase bed stresses and generate a cross-shore exchange flow causing offshore sediment transport (Flores et al., 2017, 2020; Horner-Devine et al., 2017; Rijnsburger et al., 2018).

Recently, Rijnsburger, Flores, Pietrzak, Horner-Devine, et al. (2021) showed that tidal plume fronts from the Rhine are trapped in the mid-field plume region for more than one tidal cycle by a combination of tidal straining, advection, and a strong anti-cyclonic surface re-circulation. The tidal plume front is released from the river mouth after ebb, initially advected offshore by tidal straining, and then advected northwards on the flood by strong tidal currents. It is then carried shorewards into shallow coastal waters by cross-shore tidal straining, before being advected southwards toward the newly forming tidal plume front on the ebb. In the Rhine system, Rijnsburger, Flores, Pietrzak, Horner-Devine, et al. (2021) found that tidal advection is typically greater than the frontal propagation speed. Consequently, the surface recirculation keeps the tidal plume fronts within a distance of 15–20 km from the river mouth resulting in a multi-frontal system (e.g., Figure 1).

In their simulations, Rijnsburger, Flores, Pietrzak, Horner-Devine, et al. (2021) observed that the frontal Froude number decreased as the front was carried northward with the flood tide and then increased during the transition from flood to ebb tide. They suggest that the re-strengthening is the result of cross-shore tidal straining, which peaks during the flood-ebb transition (de Boer et al., 2008). We also note here that the frontal re-strengthening observed at the ebb-flood transition occurs when the front is propagating shoreward into shallower water. This may also contribute to an increase in the frontal Froude number as observed by Solodoch et al. (2020). The present study builds on the work of Rijnsburger, Flores, Pietrzak, Horner-Devine, et al. (2021), testing whether the variations in frontal strength can explain the observations of multiple ISW packets (Figure 1)

Long internal waves (2.5–5 km wavelength) have been observed at the mouth of the Rotterdam Waterway (van Alphen et al., 1988). However, no field observations have previously reported front-generated ISWs in the Rhine ROFI, despite several extensive field campaigns (van Alphen et al., 1988; Joordens et al., 2001; Simpson et al., 1993; Simpson & Souza, 1995). Strong mixing from wind, tidally driven bed stresses, and internal shear from tidal straining were thought to preclude their generation. In addition, most field studies were carried out 30–70 km downstream in the far-field plume (Huthnance, 1997; Rijnsburger et al., 2016; Simpson & Souza, 1995) where tidal straining is known to dominate.

In this study, we demonstrate that tidal plume fronts in a high Stokes number river plume can generate multiple ISW packets. We use field data, together with non-hydrostatic and hydrostatic numerical model data to investigate the processes responsible for their generation. In Section 2, the methods are presented. In Section 3, we sequentially present the analysis of the satellite image of ISWs (Figure 1 and Section 3.1), in-situ data (Flores et al., 2017, 2018; Horner-Devine et al., 2017; Rijnsburger et al., 2018), an idealized two-dimensional non-hydrostatic model (Section 3.3) and a realistic three-dimensional hydrostatic model (Section 3.4 and 3.5). We then discuss the generation mechanism of the different ISW packets. In Section 4, we explore how the Rhine ROFI ISWs differ from other tidal plume systems, such as the Columbia River plume and conclude the study with Section 5.

2. Methods

2.1. Observations

Field measurements were conducted during fall 2014 within the Rhine River plume as part of the STRAINS II campaign (Stratification Impacts Near-shore Sediment) (Flores et al., 2017, 2018; Rijnsburger et al., 2018). Here, we focus on data from a mooring site 10 km northeast of the river mouth and 6 km offshore, at a depth of 18 m (Figure 1, black dot). The mooring consisted of an upward-looking four beam RDI Workhorse acoustic doppler current profiler (ADCP) with a sampling frequency of 1 Hz and vertical bins of 0.25 m. We applied a running average of 30 s with steps of 10 s to the ADCP data to filter out surface waves. In addition, four Seabird Microcat conductivity temperature depth (CTD) instruments were at depths of 1, 2.5, 10, and 15 m below the surface with sampling periods between 20 and 50 s.

Since the CTD data did not have the spatial or temporal resolution to fully resolve the ISWs we reconstructed the isopycnals using the vertical velocity measured by the ADCP, resulting in an estimation of wave amplitude and period. The ADCP acoustic backscatter signal is used to verify these reconstructed isopycnals. In addition, we used the velocity data to estimate wave direction. First, we applied a highpass Butterworth filter with a filter time of 45 min to remove the background flow. Then, wave direction was estimated using the filtering method of Mirshak and Kelley (2009) around the core of the internal wave signal. The high frequency data was rotated in the estimated wave direction to obtain wave velocities.

The speed and direction of the freshwater front was obtained by using the acoustic backscatter signal of the ADCP data (Li & Pawlowicz, 2018; Mirshak & Kelley, 2009; Scotti et al., 2005). First, a cross-correlation was applied to the intensity signal of the ADCP data to obtain the time lag ($\delta \mathrm{T}_{i,j}$) between the different beams. Second, the speed (C_p) and direction (θ) of the front was related to this time lag by

$$\delta T_{i,j} = \frac{X_{i,j}\cos(\theta - \beta_{i,j})}{C_p}, \tag{1}$$

where i, j refer to the different beams, and $X_{i,j}$ and $\beta_{i,j}$ are the horizontal distances and angles between beams i and j. We shifted the obtained time lag by ± 2 seconds to estimate the sensitivity of the calculation to the time lag, and therefore the possible increase and decrease in frontal speed.

2.2. Non-Hydrostatic Numerical Model

Two-dimensional non-hydrostatic simulations were carried out with the Internal Gravity Wave model (Lamb, 1994, 2007). This model solves the fully nonlinear, non-hydrostatic Boussinesq equations. The numerical scheme uses a second-order Godunov upwind scheme with a monotonized slope computation which provides selective numerical dissipation and diffusion near sharp gradients. This damps energy accumulation at small scales. We used a constant water depth of 18 m with vertical and horizontal resolutions of 0.09 and 1 m, respectively. Rotational effects were included using the f-plane approximation with $f = 1.15 \cdot 10^{-4}\ s^{-1}$. The model was initialized with a density field based on the field-data and the front is driven by a prescribed vertically sheared inflow with lighter near-surface water (Figure 2). The inflow consisted of a vertically uniform current u_0 and a surface current u_s. The uniform current was included to eliminate the formation of overturns at the inflow (left) boundary and did not have a physical meaning. The inflow was increased linearly over 1,200 s. Results were plotted in a reference frame moving with speed u_0. The in-flowing surface current behind the front was $u_s \approx 0.23$ m/s, and the uniform current was $u_0 \approx 1.12$ m/s. This model set-up did not include tidal currents and bottom friction.

2.3. Hydrostatic Numerical Model

We used the three-dimensional hydrostatic numerical flow-model Delft3D to obtain spatial fields of density and currents for the period of the field campaign (e.g., Deltares, 2014; Stelling & Van Kester, 1994). The model covered the entire southern North Sea by using four grids with increasing horizontal resolution toward the coast, with coastal area grid cells of about 80–500 m and 80–400 m in the cross shore and alongshore directions. The model had 20 non-equidistant sigma-layers in the vertical with smaller cells near the surface and the bottom. It was forced by water levels constructed from 50 tidal constituents at the

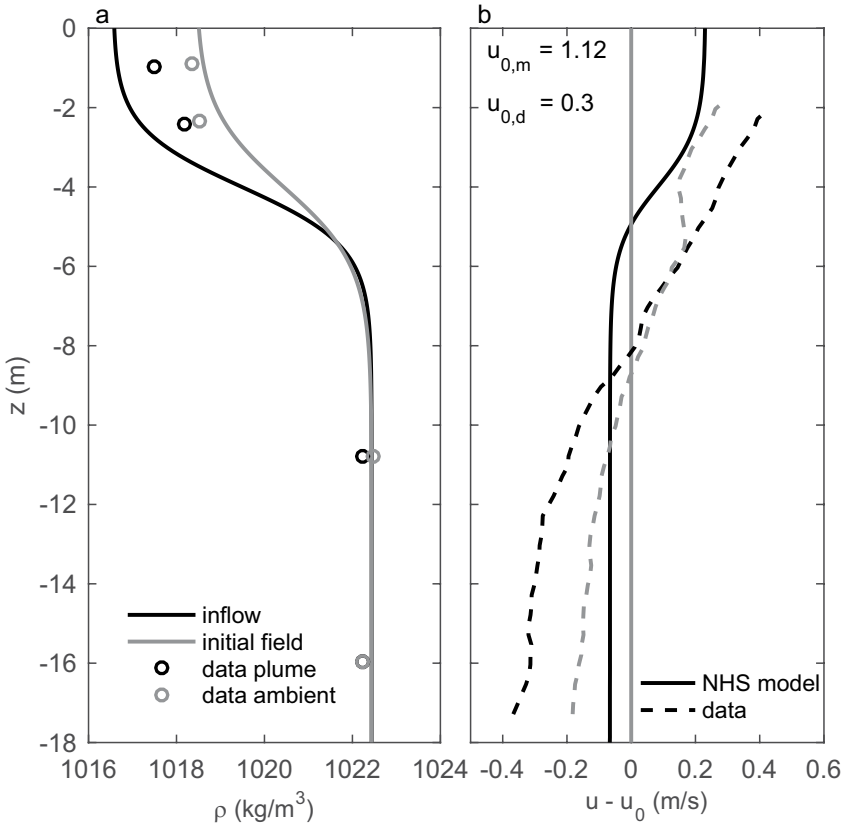

Figure 2. Non-hydrostatic model set-up based on mooring data at day 277 (October 4, 2014 around 10:43). (a) Profiles of initial density (gray line) and inflow density (black line). (b) Profiles of initial current (gray) and inflow current (black). The current is plotted in a reference frame moving with a vertically uniform current u_0 ($u - u_0$). Corresponding field-data has been plotted for both the density (circles) and velocity (dashed line), where black is behind the front and gray is ahead of the front (in ambient). $u_{0,m}$ and $u_{0,d}$ refer to the depth averaged ambient current in the model and data, respectively.

boundaries, space- and time-varying meteorological fields, and time-varying discharges for 85 rivers among which the Meuse and Rhine Rivers are the most important. Additionally, realistic bathymetry was used, and the model was initialized with uniform salinity and temperature values of 34.5 psu and 11°C, respectively (Suijlen & Duin, 2002).

Passive tracers, similar to dye injection, were added to the model to follow the freshwater outflow and tidal plume front. Each tracer patch was released between 2 h before and 2 h after low water with an initial concentration of 1 kg/m^3. The timing of low water was determined using the dominant M2 tidal constituent.

As Delft3D is a hydrostatic numerical model it cannot simulate ISWs but does capture the fronts. This is in agreement with Ralston et al. (2017) who showed that a hydrostatic numerical model can be used to resolve sharp gradients when horizontal and temporal resolution is sufficient. Validation of the model demonstrated that it captures tidal, wind, and buoyancy-driven flow, including tidal plume fronts (Rijnsburger, Flores, Pietrzak, Horner-Devine, et al., 2021).

3. Results

Herein, we first present both the satellite image (Section 3.1) and in-situ measurements (Section 3.2) that demonstrate the presence of multiple ISWs in the plume mid-field. An example in-situ observed tidal plume front and its associated ISWs are selected for a detailed analysis. We then present the results of two- and three-dimensional numerical studies to further interpret the observations. First idealized two-dimensional non-hydrostatic numerical simulations are used to illustrate the mechanism for the generation of the

ISWs (Section 3.3). ISWs can only propagate ahead of the front of the frontal Froude number is subcritical. Finally, a three-dimensional hydrostatic model is used to study the tidal plume fronts, and the evolution of Froude numbers in time and space (Section 3.4 and 3.5). Based on these results, a mechanism for the formation of multiple ISW packets is proposed.

3.1. Satellite Observations of Internal Solitary Waves

We investigated whether the multiple ISW packets observed in Figure 1 could have been generated by the same tidal plume front. The Copernicus Sentinel-2 data in Figure 1 has a spatial resolution between 10 and 60 m. The image shows the presence of multiple fronts (white thin lines), not all of which are associated with ISW packets. Four ISW packets and the tidal plume front are highlighted in the satellite image (Figure 1), where packet A seemed to be released by the front with a distance of 0.65 km to the leading wave. Figure 1 shows that the front is approximately 5.8 km from the river mouth. Figure 1 also shows packets B, C, and D that are approximately 4.2, 8.6, and 10.3 km from the front.

In previous work, we found that fronts in the Rhine ROFI have an average propagation speed of approximately 0.8 m/s relative to the ground (Rijnsburger et al., 2018). Using that value as an estimate of the propagation speed of the tidal plume front in Figure 1, we estimated that the tidal plume front, labeled in Figure 1b, had traveled for 2 h since it was released from the mouth. Therefore, for the ISW packets in Figure 1 to have been released from the tidal plume front, this must-have happened within 2 h. Additionally, these waves should have a larger speed than the tidal plume front.

Based on Nash and Moum (2005) we assumed that the ISWs propagate 0.1–0.15 m/s faster than the front. Using these speeds, a first order approximation suggests that packets A, B, C, and D are 1.2–1.8, 8–12, 16–24, and 19–29 h ahead of the front, respectively. These calculations do not take into account possible changes in speed during a tidal cycle.

The estimated travel times indicated that it is unlikely that ISW packets B, C, and D were generated by the tidal plume front highlighted in Figure 1. These packets could only be released from the current tidal plume front if they propagated much faster than the front (i.e., $\gg$0.15 m/s): for packet B we would need an ISW propagation speed of at least 0.6 m/s and at least twice that again for the other packets. As the estimated travel times of packets C and D were larger than 12 h, they were likely generated on the previous tidal cycle. Based on this analysis, we concluded that packets A, B, C, and D must have been generated by different fronts, although the satellite image does not show obvious fronts related to all the ISW packets. In the following sections, we used in-situ observations and numerical modeling to investigate this process in more detail.

3.2. In-Situ Observations of Internal Solitary Waves

Over an 18-day period, we observed 17 frontal events with ISWs at the mooring site, of which only 10 showed pronounced ISW signals (Figure 3). Of these 10 pronounced events, five were observed during low energy conditions, that is, neap tide and a relatively low wind speed directed offshore or southwards (Figure 3). The other five events occurred during variable wind and tide conditions, resulting in different stratification and frontal behavior (Rijnsburger et al., 2018). It is possible that ISWs generated at the tidal plume front did not reach the mooring site under all conditions and that under certain wind and tide conditions ISWs were either not generated or were quickly destroyed.

ISW events commenced between 5 and 70 min before and within 5 min after frontal passage. The first observed wave was marked by an X, and a differentiation was made between before and after the front (Figure 3b). This definition resulted in a maximum of two X's per frontal event (Figure 3b). Waves appeared more often before the front than after (Figures 3b and 3c). The event-averaged top to bottom density difference $\Delta\rho$ in the ambient waters was about 3 ± 1 kg/m^3, while within the plume it was 6 ± 1 kg/m^3. $\Delta\rho$ ahead of the front was quite variable (Figures 3b and 3c), indicating a wide range of background conditions.

We focused on one frontal event, day 277.44 (black triangle in Figure 3b) when a 70 min period of ISWs was observed before frontal passage (Figure 4). The presence of the waves and the freshwater front was captured in the acoustic backscatter (Figure 4a). The event had clear downwelling and upwelling at the frontal head

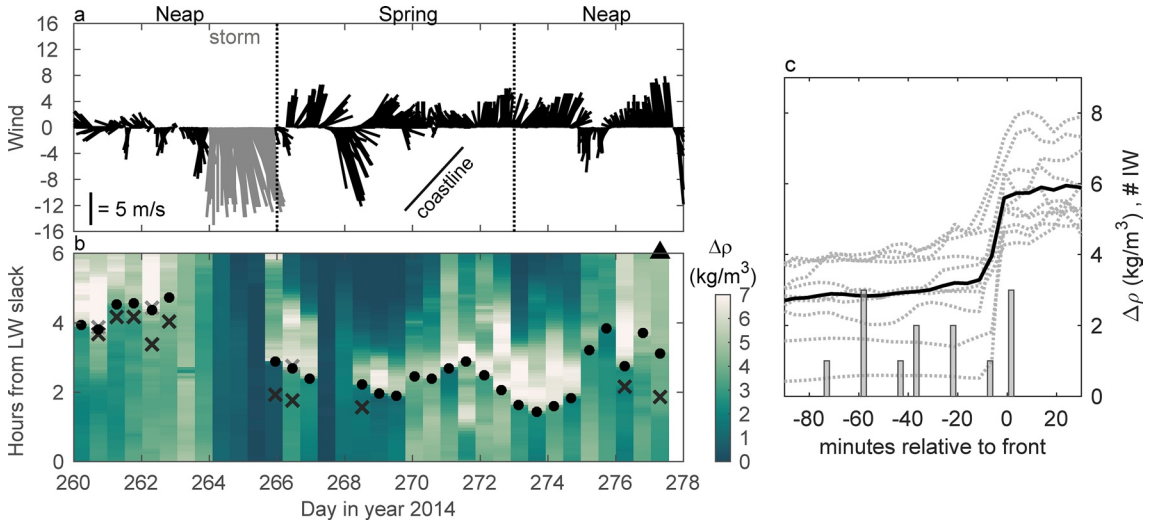

Figure 3. Internal solitary waves (ISW) events at the 18 m mooring site. (a) Wind vectors (m/s). Spring, neap, and storm periods are highlighted above the panel. The direction of the coastline is also indicated. (b) Density difference (color, bottom–top) over 6 h commencing at low water slack for the entire period in days of year ($t = 0$ is slack water). The black dots indicate the arrival of the fronts, the black X is the first observed ISW ahead of the front and the gray X is the first ISW behind the front. Note that the X only indicates the first wave observed ahead or behind the front. The black triangle indicates the example plotted in Figure 4c. Density difference and number of ISW events (gray bars) versus minutes relative to the front in bins of 5 min. The black line is the density difference averaged over the 10 tidal cycles (gray dotted lines) where ISWs were observed (see panel b). The histogram shows the start time of the internal wave event relative to the front and the occurrence during the campaign.

as expected for gravity currents (Britter & Simpson, 1978), and an estimated frontal speed of 0.76 m/s. Only a small density difference was observed at front arrival (Figure 4b, time indicated by the rightmost dot at the top of panel a). In addition, the front normal velocity highlighted the presence of the plume, which had increased surface velocities compared to the ambient waters ahead and below. Many ISWs of depression are present (Figure 4).

Figures 4e–4g zooms in on three ISWs for which we estimated amplitudes between 2 and 3.5 m (crest to trough), and periods of 3.5, 2.5, and 2 min, respectively. The ISW induced currents (Figures 4e–4g) were obtained using the filtered velocity data (Section 2.1). They showed periods of convergence at the leading edge and divergence at the trailing edge of the ISWs, resulting in downwelling and upwelling, respectively (Figures 4d–4g). In addition, there are oppositely directed surface and bottom currents. Notably, the ISWs 45–70 min before the front (09:25–10:00) had a longer period than the waves between 0 and 45 min before the front (10:00–10:45) (Figure 4, dot 1 and dot 2 at the top of panel a). In addition, the front normal velocity suggested that a small change in pycnocline depth occurred at approximately 10:00 (Figure 4c, the light red band starting at 15 and 16 m, respectively). No large change in surface density was observed at this time (Figure 4b).

Internal wave packets are generally formed by the nonlinear dispersive evolution of a disturbance (Helfrich & Melville, 2006). The propagation speed of ISWs increases with wave amplitude. Therefore, these waves typically evolve into a rank-ordered packet of ISWs with gradually decreasing amplitude from the front to the back of the packet. However, an abrupt change in the properties of the waves was observed at around 10:00 (Figure 4). The waves before 10:00 appeared to be rank-ordered larger period ISWs, while after 10:00 the waves appeared to be smaller amplitude, more sinusoidal, and smaller period waves that are not clearly rank-ordered. Therefore, the data suggested that two different wave packets, with different properties, were observed. This appeared to have some similarities with the satellite image (Figure 1). Two other events displayed similar behavior with abrupt changes in ISW properties before the front arrival. Each of these events had a corresponding change in the pycnocline depth, and no large change in surface density (days 262.48 and 266.57, not shown here).

In the following sub-sections, we use numerical modeling to shed light on the observations and based on this suggest a mechanism for the formation of multiple ISW packets.

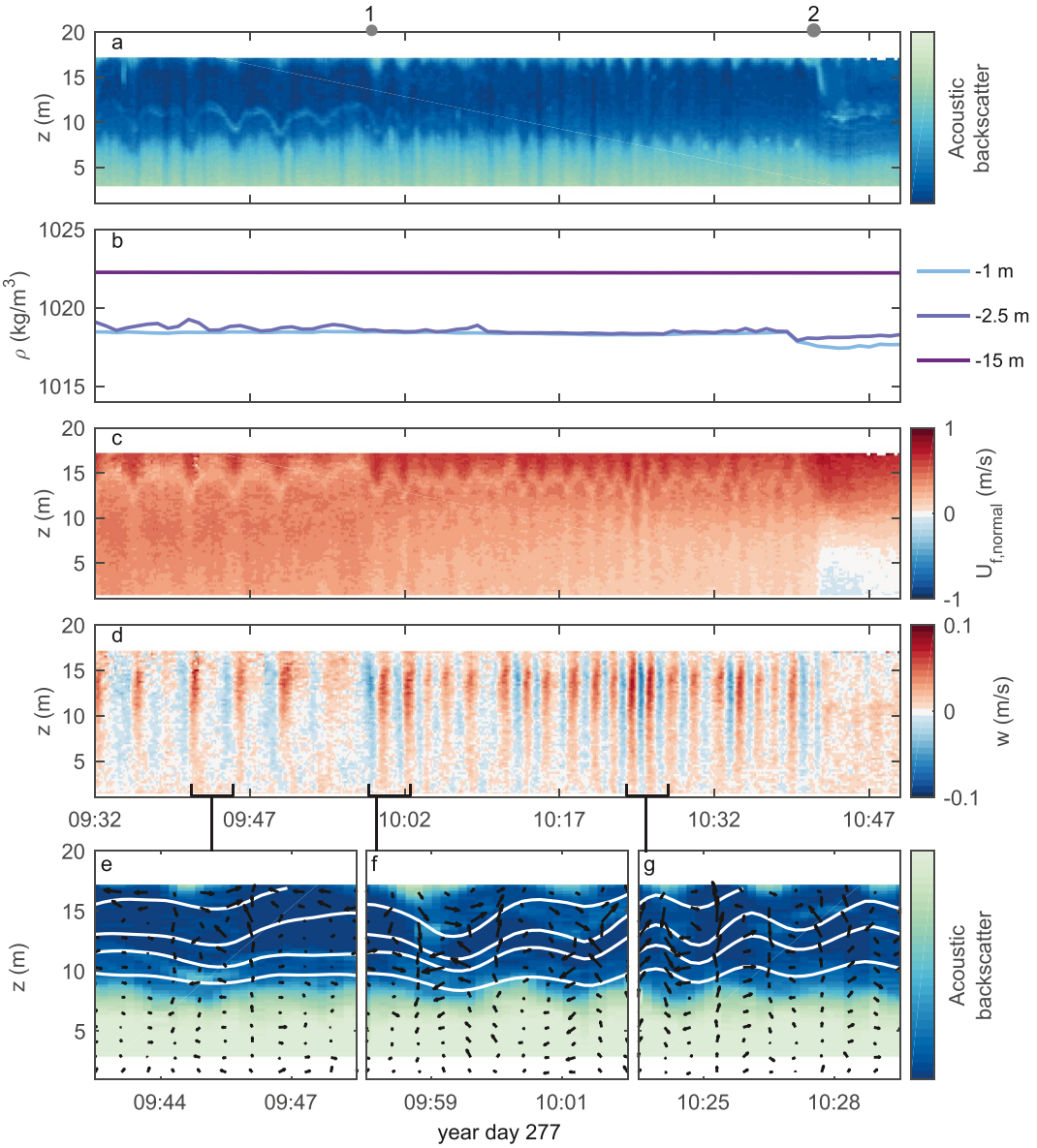

Figure 4. Internal solitary waves example on day 277 (October 4, 2014). (a) Acoustic backscatter signal from the acoustic Doppler current profiler at the mooring site (b) Density at three different heights in the water column, −1 m, −2.5 m, and −15 m. (c) Front normal velocity (m/s), where positive values indicate flow in the direction of frontal propagation. (d) Vertical velocity w (m/s), where upward is positive. (e)–(g) represent three internal wave events of 5 min, where color represents acoustic backscatter. White lines are reconstructed isopycnals, velocity vectors represent the wave-induced currents. The gray dots represent (1) 10:00 and (2) 10:43 arrival of the tidal plume front.

3.3. Non-Hydrostatic Numerical Model Simulations

We carried out non-hydrostatic numerical model simulations to obtain further evidence that the tidal plume front is able to release ISWs as suggested by the field data. Given the complexity of the region, the analysis used an idealized two-dimensional simulation based on the in-situ density observations (Figure 2). We plotted the density, horizontal and vertical velocity at two moments in time, 45 and 90 min after initialization (Figure 5). We observed similarities with the field-data (Figures 2 and 4). A clear surface front was formed that thinned during propagation (Figure 5). At the same moment, a strong vertical shear of the horizontal velocity formed, with the bottom and surface currents in opposite directions. The vertical velocity showed

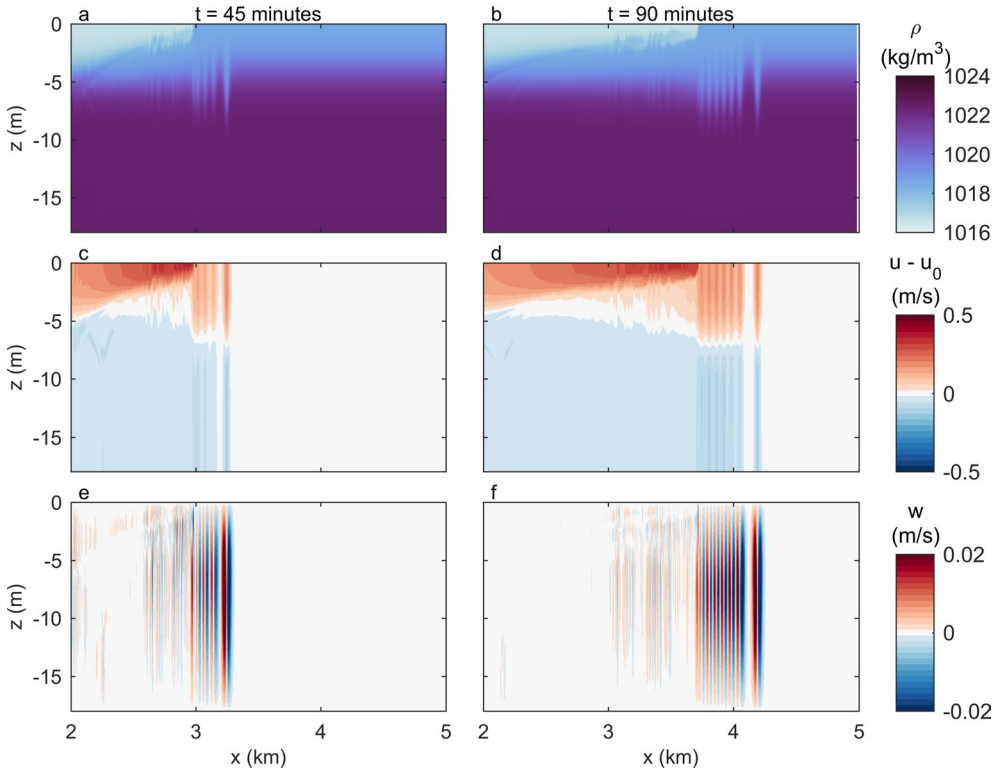

Figure 5. Non-hydrostatic model results of frontally forced internal solitary waves at two different times. (a) and (b) Density, (c) and (d) Horizontal velocity, (e) and (f) Vertical velocity. The results are plotted in a reference frame moving with background current u_0. The first column represents 45 min (a, c, e), and the second column 90 min (b, d, f) after initialization.

downwelling followed by upwelling at the tip of the front as observed in the field-data. One difference with the field-data was that the idealized model seemed to form a thinner front.

In the simulation, ISWs were continually emitted from the front and propagated ahead of it. The first two ISWs had amplitudes of ∼3 and 2.5 m (maximum isopycnal displacement). The larger leading ISW was generated as the inflow commenced and was likely an artifact of the startup procedure. Relative to the fluid ahead of it, the front propagated with a speed of about 0.23 m/s, and the first and second ISWs had propagation speeds of about 0.35 and 0.34 m/s, respectively. The propagation speed of about 0.12 m/s relative to the front agrees well with the estimate of 0.1–0.15 m/s estimated in Section 3.1. Excluding the leading ISW, the trailing ISWs were separated by about 60 m with a period of ∼3 min. Behind the front, there were much shorter periods and smaller amplitude oscillations. This idealized simulation showed that the tidal plume front is able to generate ISWs, supporting the field-data.

The Rhine ROFI contains background shear due to the counter rotating tidal currents. These tidal currents have not been taken into account in the idealized non-hydrostatic model, which was only forced by the density data. Adding such a sheared background current will change the result of the idealized numerical model, although we expect that it will mainly change the properties of the ISWs and the propagation speed of the front as shown by Pan and Jay (2009b). We still expect to observe the generation of ISW packets as suggested by the field-data. Additionally, the idealized simulation was based on the tidal plume front observed in the field-data (Figure 4, dot 2). The horizontal density gradient at the surface was roughly 2 kg/m^3 (Figure 2), suggesting that fronts do not need a large horizontal density gradient to release ISWs. The Froude number associated with the front is an important parameter for determining whether or not ISWs can be released to propagate ahead of it. This is explored in the next subsection.

3.4. Frontal Froude Number

Previous studies have demonstrated that tidal plume fronts can release ISWs if a frontal Froude number criterion is met (Nash & Moum, 2005; Stashchuk & Vlasenko, 2009). Therefore, we estimated the linear longwave phase speed ahead of the front (c_a), which is the ISW propagation speed in the limit of zero wave amplitude. To do this we used the Taylor Goldstein (TG) equation with observed 5 min averaged density and velocity profiles (Platell, 2019). A hyperbolic tangent fit was applied to the scarce density data to obtain a continuous density profile. We chose a hyperbolic tangent fit because of the good agreement in the Rotterdam Waterway (Pietrzak et al., 1990). The linear longwave phase speed ahead of the front was estimated as 0.81 m/s relative to the ground, and therefore exceeded the frontal speed. This resulted in a frontal Froude number, $F = u_f / c_a < 1$, that is, subcritical flow similar to Nash and Moum (2005). This result suggested that the front was able to release ISWs.

A 3D hydrostatic numerical model (Delft3D) was used to simulate the tidal plume fronts and estimate the temporal and along front variations of the frontal Froude number in order to identify locations where ISW packets might be released. Comparison of the field-data and the numerical model at the mooring station showed a good correspondence between the front normal velocity and the surface and near bottom density (Figures 4b and 4c and Figure 6). The vertical profiles of density supported the hyperbolic tangent fit on the field-data (Figures 6c–6f). We used the model to follow the tidal plume front in time and space, from the river mouth to the mooring station, and defined a front trajectory (see Figure 7). We identified the front using the horizontal density gradient and selected a point on the front that we then followed moving with the front normal velocity (Figure 7a, gray dots). We used the horizontal density gradient to verify that we were successfully tracking the front. We calculated Froude numbers on the front trajectory as $F = (u_f - \overline{u_a}) / (c_a - \overline{u_a})$, where u_f is the surface velocity, c_a the linear phase speed ahead of the front, and $\overline{u_a}$ the depth mean current ahead of the front.

We followed three locations of the tidal plume front (Figures 7a and 7d), identified by the gray dots, for four to six hours. All three tidal plume front trajectories showed a transition from supercritical to subcritical flow (dark to light green, Figures 7a and 7d). Trajectory II transitioned first around 09:24 followed by I around 10:00 and III around 11:16, suggesting that the release of ISWs from the tidal plume front had occurred. In addition, this result suggested that the properties of the tidal plume front changed along the front and consequently were able to release ISWs at different moments in time.

3.5. Mechanism Explaining Multiple ISW Packets

The field-data from day 277 suggested the presence of two different ISW packets due to an abrupt change in wave period and pycnocline depth around 10:00. We used the hydrostatic model to understand what process is responsible. One possibility is the generation by a front other than the current tidal plume front; however, the hydrostatic model did not show a clear surface density gradient propagating through the mooring site around this time. The horizontal density gradients did, however, show the presence of multiple fronts at other locations (Figure 7a).

We followed the tidal plume front (F0 and F2) released the previous day at two locations (gray dots) to observe their trajectory in time and space (Figure 8). Tracer concentrations of the corresponding ebb releases separated the previous from the new tidal plume front (Figures 8e–8j). The front trajectories at the locations of the gray dots (gray lines) showed that these fronts were still visible at the end of the ebb tide when a new front (F1) had already formed (Figures 8c and 8d).

The two tracer concentrations clearly explained some of the fronts visible in the density gradient, such as the current tidal plume front (F1) and the previous tidal plume front (two parts of which are labeled F0 and F2). We used the model to trace front F2 and calculated the Froude number along the trajectory (trajectory IV; Figures 7b and 7e). Trajectory IV showed a transition from super-to subcritical around 07:56, roughly after 9.5 h, which suggests that this front can release an ISW based on the theory of Nash and Moum (2005).

As previously presented, an abrupt change in ISW properties was observed around 10:00 (Figure 4). We expected to observe a front propagating through the measurement site at that moment in time, but the horizontal density gradient did not show this in the field- and hydrostatic model data. However, the hydrostatic

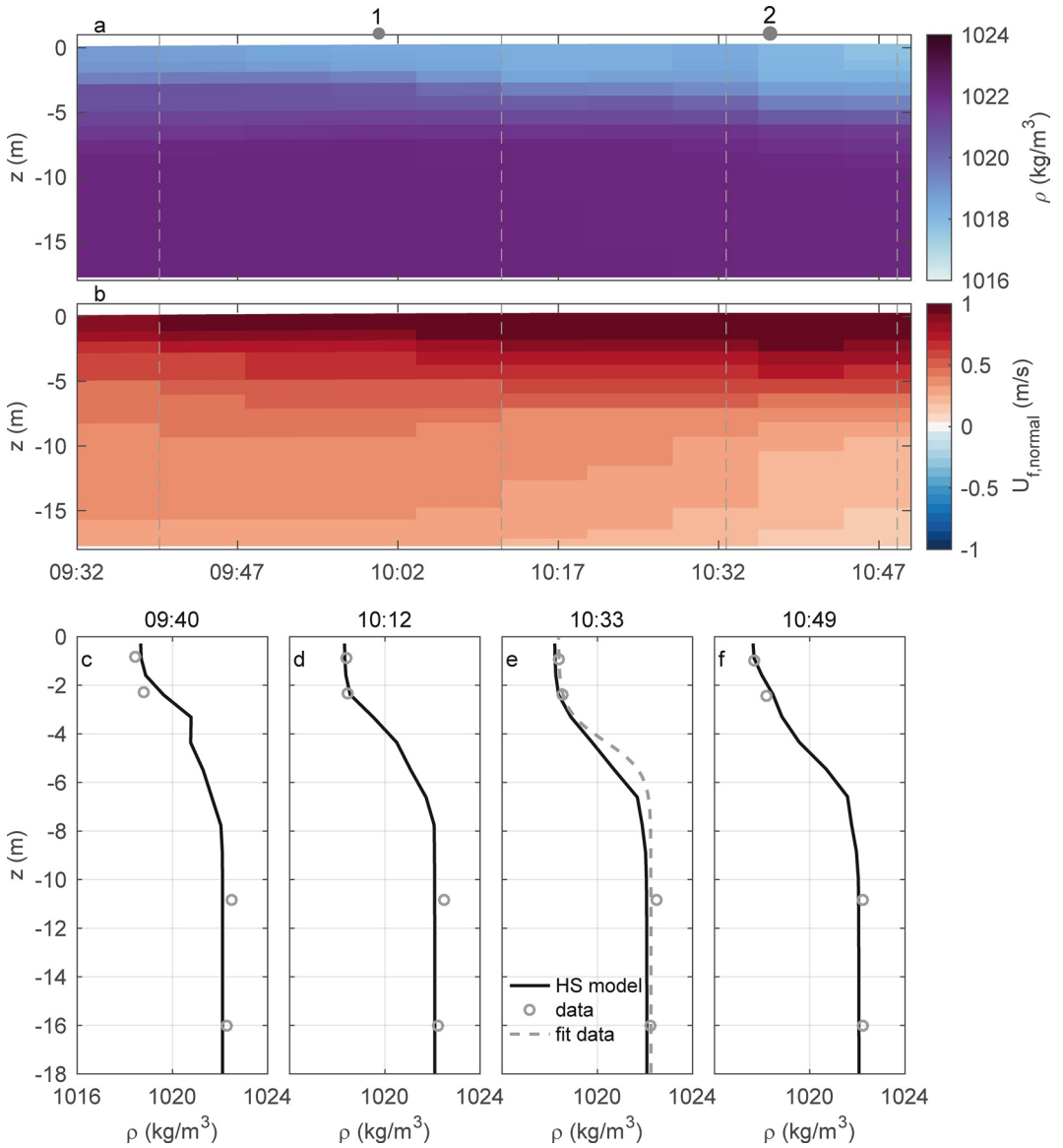

Figure 6. Time series of (a) Density and (b) Front normal velocity of the hydrostatic numerical model (HS) around the location of the mooring station. The gray dashed lines correspond to the four density profiles over depth in panels (c–f), where the black line is the HS model data, the gray circles the field-data and the gray dashed line the fit to the field-data. The number 1 corresponds to the change in water properties around 10:00 and number 2 to the arrival of the tidal plume front around 10:36–10:43.

model did show a clear horizontal density gradient at 3–4 m below the sea surface (Figures 6 and 7), suggesting the presence of a front at depth (F3). Therefore, we investigated this front in more detail, followed its trajectory, and calculated Froude numbers. The density profiles showed that after 10:00 the fresh upper layer thickened from roughly 3–4 m below the sea surface, coinciding with an increased pycnocline depth observed in the field-data (Figure 6). This thicker layer formed a horizontal density gradient at 3–4 m below the sea surface (layer five in the model) that moved toward the mooring station (Figure 7c). This front was difficult to follow, and we only managed to follow it close to the mooring station for 2 h where the Froude number remained subcritical (Figure 7f). A transition from super-to subcritical was not observed, but the front was subcritical suggesting ISWs could be released.

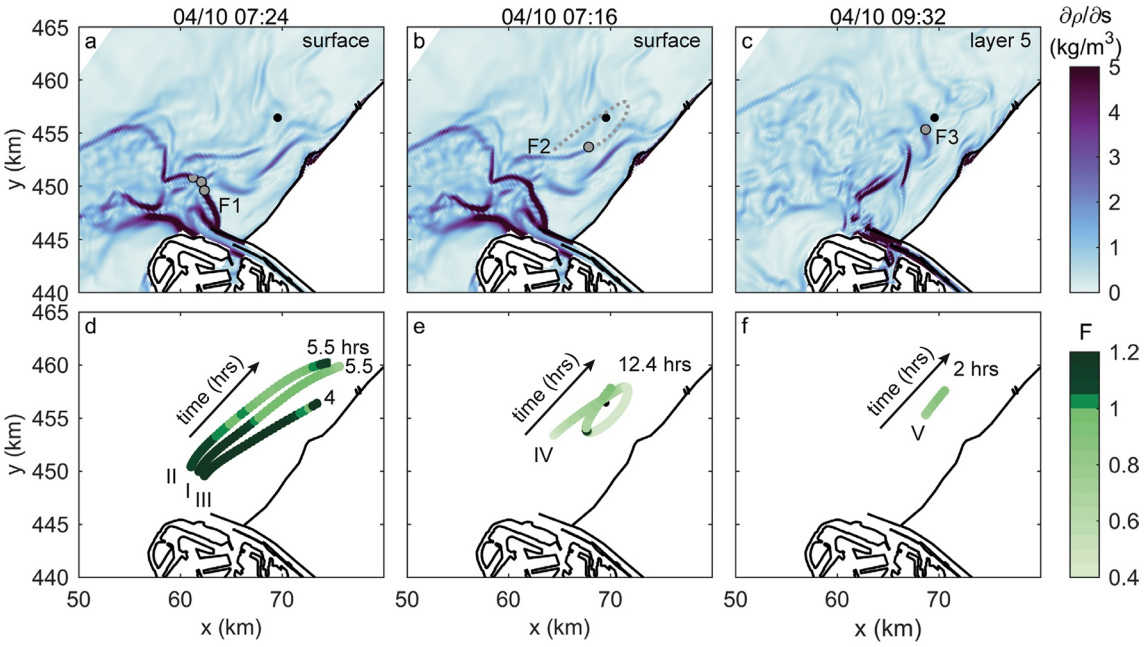

Figure 7. Spatial fields of the horizontal density gradient and Froude numbers predicted by the hydrostatic numerical model for day 277.4 (October 4, 2014). (a–c) horizontal density gradient at the surface layer or the fifth layer. The gray dots are the location of the fronts at a given moment in time and correspond to the different front trajectories in the panels beneath. The fronts are labeled F1–F3. Panel b represents a front that has already propagated for some time, its trajectory beforehand is indicated with the dotted gray line. (d–f) Front trajectories in time and space where color indicates the Froude number. The trajectories correspond to the dots in (a–c). The numbers indicate the duration of the trajectory in hours (hrs). The *x* and *y* axes are displayed in the Dutch national coordinate system (Rijksdriehoek coordinates).

4. Discussion

In this study, we observed multiple internal wave packets propagating ahead of the Rhine River tidal plume front in both in-situ data and satellite imagery. Both hydrostatic and non-hydrostatic models were used to explore their generation mechanism. On day 277.44, we observed two distinct packets of waves, with longer period waves between 09.25 and 10:00 preceding shorter period waves between 10:00 and 10:42 (Figures 4e–4h). Different front trajectories indicated that the ISW packets were generated by different fronts, as the horizontal density gradient showed a multi-frontal system (Figure 7). Using the hydrostatic model, we estimated the expected arrival time of an ISW released by each of these trajectories and compared these with the observed ISW packets. This resulted in a figure that summarizes the information obtained from these two data sources and illustrates the possible generation mechanism (Figure 9).

Trajectories I–III are related to the same tidal plume front, which is labeled as F1 (Figures 7 and 8). Trajectory I transitioned about 2 km from the mooring station, with an average u_f of 0.9 m/s and c_a of 0.93 m/s. This would lead to a predicted arrival time of an ISW around 10:30 and the front around 10:35 (Figure 9a). An ISW released by trajectory II would be predicted to arrive around 10:40 at the mooring site (about 4 km, $c_a \approx$ 0.95 m/s), while an ISW released by trajectory III would not reach the mooring site. These estimates suggest that the shorter period waves (packet 2) were likely released by the new tidal plume front F1 (Figure 9a).

An ISW released by trajectory IV, which was related to the previous tidal plume front F2, would be predicted to arrive around 09:20 at the mooring station (about 2.6 km, $c_a \approx 0.88$ m/s). The corresponding front will arrive 10–15 min later. If we assume that an ISW was released at the start of trajectory V, it would arrive at the mooring roughly between 09:56 and 10:04. The longer period waves in the observations (packet 1) were observed between 09:32 and 10:00, suggesting that the trapped front F2 (trajectory IV) theoretically could have released these ISWs (Figure 9a). It should be noted that we used the linear long wave phase speeds (c_a), calculated with the Taylor Goldstein equation, to estimate ISW propagation speed and arrival time.

These simple calculations suggest that both the new and the previous tidal plume front released internal waves, explaining the observed multiple internal wave packets (Figure 9b). The in-situ data only captured

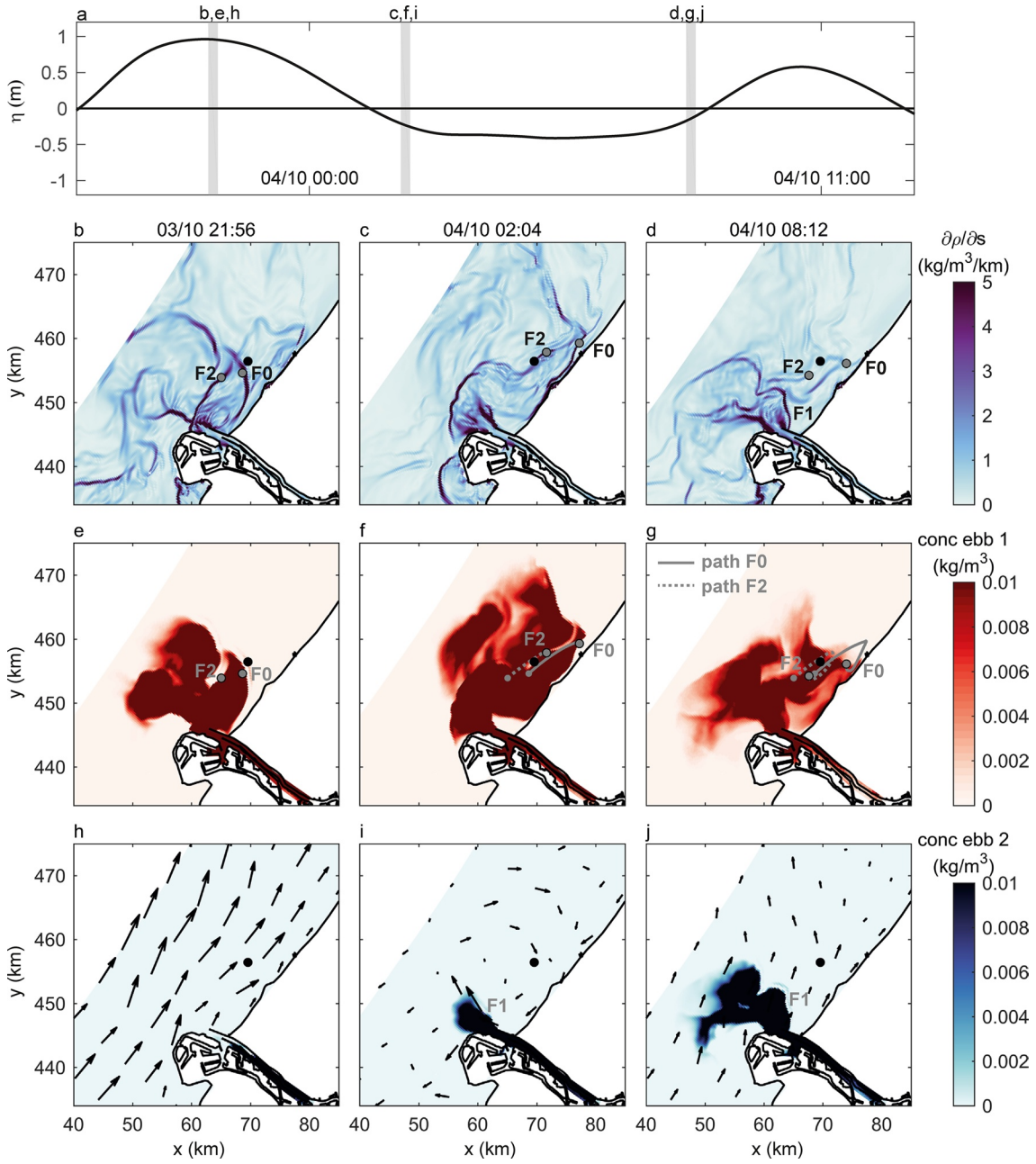

Figure 8. Trapping of tidal plume fronts using the hydrostatic model. (a) Tidal cycle showing the location of each panel in time. Plan view of absolute value of the horizontal density gradient (b)–(d), and tracer concentrations (kg/m^3) in the surface layer of two freshwater releases (October 3, 2014 and October 4, 2014), referred to as concentration ebb 1 (e)–(g) and ebb 2 (h)–(j). Each column is at a fixed time. The vectors represent surface velocity (m/s). The black dot indicates the mooring site. F0 refers to the tidal plume front formed on 03/10/2014, F1 refers to the front formed on October 4, 2014, and F2 refers to a front related to the release on 03/10/2014. The gray dots (b)–(g) mark locations on fronts F0 and F2. The trajectories of these points, moving normally to the front, are shown by the lines, where solid is front F0 and dotted is front F2. The small gray dot (e)–(g) refers to the starting point of the trajectory back in time. The *x* and *y* axes are displayed in the Dutch national coordinate system (Rijksdriehoek coordinates).

two ISW packets, while four packets were visible on the satellite image. These observations are not contradictory as the data were from different days. In the satellite image, Packet A was generated by the new tidal plume front, while packet B was likely generated by a previous tidal plume front. Packets C and D were likely released by a previous tidal plume front during the current tidal cycle in the same manner as packet B. However, the simplified calculation in Section 3.1 suggested that these two packets could have

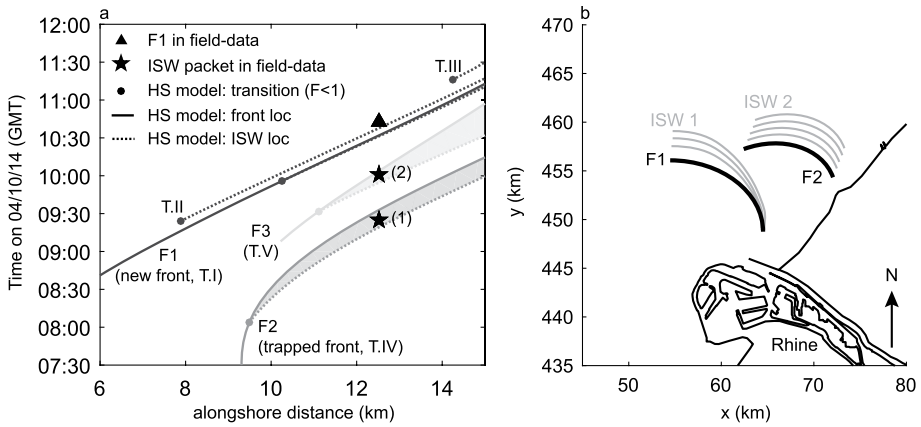

Figure 9. Summary of the evolution of the fronts and internal solitary waves (ISWs) in time. (a) Location of front and ISWs in time and space, where the black triangle and stars represent the information from the field-data, and the lines represent the information obtained from the hydrostatic model. The black triangle is the location of the tidal plume front, and the stars are the location of the ISW packets (1 and 2). The solid lines represent the location of front F1 (dark gray), front F2 (middle gray), and front F3 (light gray) in time, while the dashed line is the estimated location of released ISWs. The area inbetween is shaded. The gray dots refer to the location, where the Froude number transitioned to F < 1, indicating the release of ISWs. The location of the front and ISW in the model (lines) are based on the trajectories I–V (T.I–T.V; Figure 7) (b) Schematic of the release of multiple ISW packets due to the trapping of tidal plume fronts.

been released on the previous tidal cycle as well. Clarification on the source of four concurrent ISW packets requires further research.

Front-generated ISWs have been observed in other river plume systems, such as the Columbia River plume (Nash & Moum, 2005). However, a key difference between the Rhine and the Columbia River plume is the number of observed ISW packets. In the Rhine River plume multiple ISW packets were observed, while in the Columbia River plume only one ISW packet per tidal cycle has been observed (Jay et al., 2009; Nash & Moum, 2005; Pan et al., 2007). This difference is due to the presence of multiple fronts in the Rhine River plume. Tidal plume fronts are kept within the mid-field for more than one tidal cycle as a result of the elliptical tidal currents and the presence of tidal straining (Rijnsburger, Flores, Pietrzak, Horner-Devine, et al., 2021). This difference can be captured by the variation in the Stokes number, which is large in the Rhine River plume (>1) indicating that the bottom boundary layer extends to the water surface. The occurrence of large Stokes numbers means that there is strong tidal mixing, in contrast to systems like the Columbia and the Mississippi. The presence of this large mixing intuitively suggests that the presence of the internal waves would be suppressed, however, the mixing is not strong enough to remove the freshwater stratification and it allows for the formation of counter rotating tidal currents, which drives tidal straining and the trapping of the fronts (Rijnsburger, Flores, Pietrzak, Horner-Devine, et al., 2021; Flores et al., 2020) may be responsible for the maintenance of multiple IWS packets.

The contrasting magnitude of the ratio of the intrinsic frontal speeds and ambient tidal currents also explains the variation in dynamic between the two systems. In the Rhine, u_f / u_a ≈ 0.5 / 1 ≈ 0.5 (de Kok, 1997; Rijnsburger et al., 2018), indicating that the newly released tidal plume front is controlled by tidal advection. In contrast, frontal propagation dominates in the Columbia River plume, u_f / u_a ≈ 0.6 / 0.2 ≈ 3 (García Berdeal et al., 2002; Hickey et al, 1998, 2005; Kilcher & Nash, 2010). Finally, the difference in the tidal regime may also explain why multiple packets have not been observed in the Columbia River plume. The tides in the Columbia are mixed semidiurnal-diurnal, whereas the North Sea is strongly semidiurnal. This suggests that the Rhine is able to generate strong fronts on successive ebbs, while for the Columbia strong fronts will be generated 25 h apart. Multiple ISW packets are likely to occur in other frictional river plume systems with semidiurnal tides, a large Stokes number, and where tidal advection dominates over the intrinsic frontal speed.

Some studies have shown that tidal plume fronts play an important role in the dispersion and transport of freshwater in coastal oceans (Hickey et al., 2010; Horner-Devine et al., 2015). The spreading of the tracers

in Figure 8 suggested dispersion by the tidal plume fronts. These tracers showed that the spreading is dependent on the tidal current. The spreading in the northeast direction (alongshore) was accelerated during the flood but inhibited during the ebb. Other studies have shown that tidal plume fronts that release ISWs, further transport and mix river plume water into the ocean (Nash & Moum, 2005; Pan & Jay, 2009a). Moreover, front generated ISWs are reported to change the plume dynamics and dissipate frontal energy (Pan & Jay, 2009a). Therefore, we would expect that the ISWs generated in this system are important for turbulence, dissipation, and transport as well. The ISWs in the Rhine River plume had a ratio of wave amplitude over water depth (η / H) of 0.04–0.08, while this ratio was estimated to be roughly 20 / 60 ≈ 0.33 to 8.5 / 136 ≈ 0.06 in the Columbia River plume (Nash & Moum, 2005; Pan et al., 2007; Pan & Jay, 2009a). Pan and Jay (2009a) estimated that the fronts play an important role in dissipating energy from the tidal plume front even for waves with an amplitude ratio as small as 0.06. This indicates that ISWs generated by the Rhine front also likely play a role in dissipating energy from the fronts. Moreover, Pietrzak et al. (1991) showed that small and short period internal waves can still be significant for the production of turbulent kinetic energy in a sheared environment and should not be neglected.

5. Summary and Conclusions

Various data sources allowed us to document the presence of multiple ISW packets in the Rhine ROFI, generated by different tidal plume fronts. Field-data showed the presence of ISWs ahead of the tidal plume front. Non-hydrostatic numerical model simulations confirmed that the Rhine River plume can generate ISWs. Analysis of a satellite image showed that the different ISW packets cannot all have been generated by the same tidal plume front; instead, hydrostatic numerical modeling showed that tidal plume fronts are sustained for longer than one tidal cycle in the mid-field river plume due to straining by the elliptical tidal currents, leading to a multi-frontal system. A Froude number analysis demonstrated that both the new and older tidal plume front are able to release ISWs. All the results together explained the formation of different ISW packets observed in the in-situ data and satellite image. The presence of multiple tidal plume fronts with associated ISW packets has not been observed before; however, multiple ISW packets likely occur in other frictional river plume systems with semidiurnal tides, a large Stokes number, and where tidal advection dominates over the intrinsic frontal speed.

Tidal plume fronts and ISWs play an important role in the dispersion and transport of freshwater in coastal oceans (Hickey et al., 2010; Horner-Devine et al., 2015; Pan & Jay, 2009a). Furthermore, the ISWs can play an important role in the dissipation of tidal fronts and hence modify the plume dynamics. Therefore, it is important to identify the presence of ISWs in river plumes.

Acknowledgments
The reviewers are thanked for their comments, which improved this manuscript. The authors would like to thank Stef Lhermitte for providing the satellite image; Richard Cooke, Christopher Balfour, and the crew of the R/V Zirfaea for their technical support during the measurements; Rijkswaterstaat for their generous and kind support; NERC for the support provided to deploy the bottom frame; and Hugo Platell for sharing his knowledge and code on the Taylor Goldstein Equation. The project is funded by the Netherlands Technology Foundation STW program project Sustainable engineering of coastal systems in Regions of Freshwater Influence (project 12682), awarded to J. D. Pietrzak and H. J. H. Clercx. R. P. Flores would like to thank the Fulbright Commission and CONICYT-Chile for the scholarship provided. K. G. Lamb was supported by a grant from the Natural Sciences and Engineering Research Council of Canada. A. R. Horner-Devine was supported by the Allan and Inger Osberg Professorship. A. J. Souza was funded by NERC through NOC National Capability funding.

Data Availability Statement

The field- and model data used in this study are published as a data set in the 4TU Center for Research Data in the Netherlands (Rijnsburger, Flores, Pietrzak, Lamb, et al., 2021).

References

Aghsaee, P., & Boegman, L. (2015). Experimental investigation of sediment resuspension beneath internal solitary waves of depression. *Journal of Geophysical Research: Oceans*, *120*, 3301–3314. https://doi.org/10.1002/2014jc010401

Baumert, H., & Radach, G. (1992). Hysteresis of turbulent kinetic energy in nonrotational tidal flows: A model study. *Journal of Geophysical Research*, *97*, 3669–3677. https://doi.org/10.1029/91jc02717

Benjamin, T. B. (1968). Gravity currents and related phenomena. *Journal of Fluid Mechanics*, *31*, 209–248. https://doi.org/10.1017/s0022112068000133

Bogucki, D., Dickey, T., & Redekopp, L. (1997). Sediment resuspension and mixing by resonantly generated internal solitary waves. *Journal of Physical Oceanography*, *27*, 1181–1196. https://doi.org/10.1175/1520-0485(1997)027<1181:srambr>2.0.co;2

Bourgault, D., Galbraith, P. S., & Chavanne, C. (2016). Generation of internal solitary waves by frontally forced intrusions in geophysical flows. *Nature Communications*, *7*, 1–9. https://doi.org/10.1038/ncomms13606

Britter, R., & Simpson, J. (1978). Experiments on the dynamics of a gravity current head. *Journal of Fluid Mechanics*, *88*, 223–240. https://doi.org/10.1017/s0022112078002074

Burchard, H., & Hetland, R. D. (2010). Quantifying the contributions of tidal straining and gravitational circulation to residual circulation in periodically stratified tidal estuaries. *Journal of Physical Oceanography*, *40*, 1243–1262. https://doi.org/10.1175/2010jpo4270.1

Da Silva, J. C., New, A. L., Srokosz, M. A., & Smyth, T. J. (2002). On the observability of internal tidal waves in remotely-sensed ocean color data. *Geophysical Research Letters*, *29*, 10–14. https://doi.org/10.52590/m3.p610.a30001046

de Boer, G. J., Pietrzak, J. D., & Winterwerp, J. C. (2008). Using the potential energy anomaly equation to investigate tidal straining and advection of stratification in a region of freshwater influence. *Ocean Modelling*, *22*, 1–11. https://doi.org/10.1016/j.ocemod.2007.12.003

de Kok, J. (1996). A two-layer model of the Rhine plume. *Journal of Marine Systems*, *8*, 269–284. https://doi.org/10.1016/0924-7963(96)00010-3

de Kok, J. (1997). Baroclinic eddy formation in a Rhine plume model. *Journal of Marine Systems*, *12*, 35–52. https://doi.org/10.1016/s0924-7963(96)00087-5

Deltares (2014). *Delft3D-flow user manual, (Technical Report)* (Vol. 3.15). Deltares.

de Ruijter, W. P. M., van der Giessen, A., & Groenendijk, F. C. (1992). Current and density structure in the Netherlands coastal zone. In: D. Prandle (Ed.), *Dynamics and exchanges in estuaries and the coastal zone*, (Vol. 40, pp. 529–550). American Geophysical Union. https://doi.org/10.1029/ce040p0529

Farmer, D., & Armi, L. (1999). The generation and trapping of solitary waves over topography. *Science*, *283*, 188–190. https://doi.org/10.1126/science.283.5399.188

Fischer, E., Burchard, H., & Hetland, R. D. (2009). Numerical investigations of the turbulent kinetic energy dissipation rate in the Rhine region of freshwater influence. *Ocean Dynamics*, *59*, 629–641. https://doi.org/10.1007/s10236-009-0187-4

Flores, R. P., Rijnsburger, S., Horner-Devine, A. R., Kumar, N., Souza, A. J., & Pietrzak, J. D. (2020). The formation of turbidity maximum zones by minor axis tidal straining in regions of freshwater influence. *Journal of Physical Oceanography*, *50*, 1265–1287. https://doi.org/10.1175/jpo-d-18-0264.1

Flores, R. P., Rijnsburger, S., Horner-Devine, A. R., Souza, A. J., & Pietrzak, J. D. (2017). The impact of storms and stratification on sediment transport in the Rhine region of freshwater influence. *Journal of Geophysical Research: Oceans*, *122*, 4456–4477. https://doi.org/10.1002/2016jc012362

Flores, R. P., Rijnsburger, S., Meirelles, S., Horner-Devine, A. R., Souza, A. J., Pietrzak, J. D., et al. (2018). Wave generation of gravity-driven sediment flows on a predominantly sandy seabed. *Geophysical Research Letters*, *45*, 7634–7645. https://doi.org/10.1029/2018gl077936

García Berdeal, I., Hickey, B. M., & Kawase, M. (2002). Influence of wind stress and ambient flow on a high discharge river plume. *Journal of Geophysical Research*, *107*. https://doi.org/10.1029/2001jc000932

Garvine, R. W., & Monk, J. D. (1974). Frontal structure of a river plume. *Journal of Geophysical Research*, *79*, 2251–2259. https://doi.org/10.1029/jc079i015p02251

Helfrich, K. R., & Melville, W. K. (2006). Long nonlinear internal waves. *Annual Review of Fluid Mechanics*, *38*, 395–425. https://doi.org/10.1146/annurev.fluid.38.050304.092129

Hessner, K., Rubino, A., Brandt, P., & Alpers, W. (2001). The Rhine outflow plume studied by the analysis of synthetic aperture radar data and numerical simulations. *Journal of Physical Oceanography*, *31*, 3030–3044. https://doi.org/10.1175/1520-0485(2001)031<3030:tropsb>2.0.co;2

Hetland, R. D. (2005). Relating river plume structure to vertical mixing. *Journal of Physical Oceanography*, *35*, 1667–1688. https://doi.org/10.1175/jpo2774.1

Hickey, B., Geier, S., Kachel, N., & MacFayden, A. (2005). A bi-directional river plume: The Columbia in summer. *Continental Shelf Research*, *25*, 1631–1656. https://doi.org/10.1016/j.csr.2005.04.010

Hickey, B., Kudela, R. M., Nash, J. D., Bruland, K. W., Peterson, W. T., MacCready, P., & Lohan, M. C. (2010). River influences on shelf ecosystems: Introduction and synthesis. *Journal of Geophysical Research: Oceans*, *115*, 1–26. https://doi.org/10.1029/2009jc005452

Hickey, B., Pietrafesa, L., Jay, D., & Boicourt, W. (1998). The Columbia River plume study: Subtidal variability in the velocity and salinity fields. *Journal of Geophysical Research: Oceans*, *103*, 10339–10368. https://doi.org/10.1029/97jc03290

Horner-Devine, A. R., Hetland, R. D., & MacDonald, D. G. (2015). Mixing and transport in coastal river plumes. *Annual Review of Fluid Mechanics*, *47*, 569–594. https://doi.org/10.1146/annurev-fluid-010313-141408

Horner-Devine, A. R., Pietrzak, J. D., Souza, A. J., Mckeon, M. A., Meirelles, S., Henriquez, M., et al. (2017). Cross-shore transport of nearshore sediment by river plume frontal pumping. *Geophysical Reseach Letters*, *44*, 6343–6351. https://doi.org/10.1002/2017gl073378

Huthnance, J. M. (1997). The PROFILE project: An overview. *Journal of Marine Systems*, *12*, 249–261. https://doi.org/10.1016/s0924-7963(96)00101-7

Jay, D. A., Pan, J., Orton, P. M., & Horner-Devine, A. R. (2009). Asymmetry of Columbia River tidal plume fronts. *Journal of Marine Systems*, *78*, 442–459. https://doi.org/10.1016/j.jmarsys.2008.11.015

Joordens, J. C. A., Souza, A. J., & Visser, A. (2001). The influence of tidal straining and wind on suspended matter and phytoplankton distribution in the Rhine outflow region. *Continental Shelf Research*, *21*, 301–325. https://doi.org/10.1016/s0278-4343(00)00095-9

Kilcher, L. F., & Nash, J. D. (2010). Structure and dynamics of the Columbia River tidal plume front. *Journal of Geophysical Research: Oceans*, *115*, 1–20. https://doi.org/10.1029/2009jc006066

Klymak, J. M., & Moum, J. N. (2003). Internal solitary waves of elevation advancing on a shoaling shelf. *Geophysical Research Letters*, *30*, 8–11. https://doi.org/10.1029/2003gl017706

Lamb, K. G. (1994). Numerical experiments of internal wave generation by strong tidal flow across a finite amplitude bank edge. *Journal of Geophysical Research*, *99*, 843–864. https://doi.org/10.1029/93jc02514

Lamb, K. G. (2007). Energy and pseudoenergy flux in the internal wave field generated by tidal flow over topography. *Continental Shelf Research*, *27*, 1208–1232. https://doi.org/10.1016/j.csr.2007.01.020

Li, L., & Pawlowicz, R. (2018). Seasonal variability and generation mechanisms of nonlinear internal waves in the Strait of Georgia. *Journal of Geophysical Research: Oceans*, *123*, 1–21. https://doi.org/10.1029/2017jc013563

Luketina, D. A., & Imberger, J. (1987). Characteristics of a surface buoyant jet. *Journal of Geophysical Research*, *92*, 5435–5447. https://doi.org/10.1029/jc092ic05p05435

Maxworthy, T. (1979). A note on the internal solitary waves produced by tidal flow over a three-dimensional ridge. *Journal of Geophysical Research*, *84*. https://doi.org/10.1029/jc084ic01p00338

Maxworthy, T., Leilich, J., Simpson, J. E., & Meiburg, E. H. (2002). The propagation of a gravity current into a linearly stratified fluid. *Journal of Fluid Mechanics*, *453*, 371–394. https://doi.org/10.1017/s0022112001007054

Mirshak, R., & Kelley, D. E. (2009). Inferring propagation direction of nonlinear internal waves in a vertically sheared background flow. *Journal of Atmospheric and Oceanic Technology*, *26*, 615–625. https://doi.org/10.1175/2008jtecho632.1

Nash, J. D., & Moum, J. N. (2005). River plumes as a source of large-amplitude internal waves in the coastal ocean. *Nature*, *437*, 400–403. https://doi.org/10.1038/nature03936

Orton, P. M., & Jay, D. A. (2005). Observations at the tidal plume front of a high-volume river outflow. *Geophysical Research Letters*, *32*, 1–4. https://doi.org/10.1029/2005gl022372

Osadchiev, A. A. (2018). Small mountainous rivers generate high-frequency internal waves in coastal ocean. *Scientific Reports*, *8*, 1–8. https://doi.org/10.1038/s41598-018-35070-7

Ostrovsky, L. A., & Stepanyants, Y. A. (1989). Do internal solutions exist in the ocean? *Reviews of Geophysics*, *27*, 293–310. https://doi.org/10.1029/rg027i003p00293

Pan, J., & Jay, D. A. (2009a). Dynamic characteristics and horizontal transports of internal solitons generated at the Columbia River plume front. *Continental Shelf Research*, *29*, 252–262. https://doi.org/10.1016/j.csr.2008.01.002

Pan, J., & Jay, D. A. (2009b). Effects of ambient velocity shear on nonlinear internal wave associated mixing at the Columbia River plume front. *Journal of Geophysical Research*, *114*, 1–13. https://doi.org/10.1029/2008jc004988

Pan, J., Jay, D. A., & Lin, H. (2009). Determining azimuthal variations in frontal Froude number from SAR imagery. *Geophysical Research Letters*, *36*(15), 1–6. https://doi.org/10.1029/2009GL039068

Pan, J., Jay, D. A., & Orton, P. M. (2007). Analyses of internal solitary waves generated at the Columbia River plume front using SAR imagery. *Journal of Geophysical Research: Oceans*, *112*, 1–11. https://doi.org/10.1029/2006jc003688

Pietrzak, J., Kranenburg, C., & Abraham, G. (1990). Resonant internal waves in fluid flow. *Nature*, *344*, 844–847. https://doi.org/10.1038/344844a0

Pietrzak, J., Kranenburg, C., Abraham, G., Kranenborg, B., & Wekken, A. V. D. (1991). Internal wave activity in Rotterdam waterway. *Journal of Hydraulic Engineering*, *117*, 738–757. https://doi.org/10.1061/(asce)0733-9429(1991)117:6(738)

Platell, H. (2019). *Internal gravity waves in the Rhine ROFI: Applicability of the KdV model (MSc. Thesis)*. Delft University of Technology.

Prandle, D. (1982). The vertical structure of tidal currents and other oscillatory flows. *Continental Shelf Research*, *1*, 191–207. https://doi.org/10.1016/0278-4343(82)90004-8

Ralston, D. K., Cowles, G. W., Geyer, W. R., & Holleman, R. C. (2017). Turbulent and numerical mixing in a salt wedge estuary: Dependence on grid resolution, bottom roughness, and turbulence closure. *Journal of Geophysical Research: Oceans*, *122*, 692–712. https://doi.org/10.1002/2016jc011738

Rijnsburger, S., Flores, R. P., Pietrzak, J. D., Horner-devine, A. R., & Souza, A. J. (2018). The influence of tide and wind on the propagation of fronts in a shallow river plume. *Journal of Geophysical Research: Oceans*, *123*, 1–17. https://doi.org/10.1029/2017jc013422

Rijnsburger, S., Flores, R. P., Pietrzak, J. D., Horner-Devine, A. R., Souza, A. J., & Zijl, F. (2021). The evolution of plume fronts in the Rhine region of freshwater influence. *Journal of Geophysical Research: Oceans*, *126*. https://doi.org/10.1029/2019JC015927

Rijnsburger, S., Flores, R. P., Pietrzak, J. D., Lamb, K. G., Jones, N. L., Horner-Devine, A. R., & Souza, A. J. (2021). *Data underlying the publication: Observations of multiple internal wave packets in a tidal river plume*. 4TU.ResearchData. https://doi.org/10.4121/14829069.v1

Rijnsburger, S., van der Hout, C. M., van Tongeren, O., de Boer, G. J., van Prooijen, B. C., Borst, W. G., & Pietrzak, J. D. (2016). Simultaneous measurements of tidal straining and advection at two parallel transects far downstream in the Rhine ROFI. *Ocean Dynamics*, *66*, 719–736. https://doi.org/10.1007/s10236-016-0947-x

Sandstrom, H., & Elliott, J. (1984). Internal tide and solitons on the Scotian Shelf. *Journal of Geophysical Research*, *89*, 6419–6426. https://doi.org/10.1029/jc089ic04p06415

Scotti, A., Butman, B., Beardsley, R., Alexander, P. S., & Anderson, S. (2005). A modified beam-to-earth transformation to measure short-wavelength internal waves with an acoustic Doppler current profiler. *Journal of Atmospheric and Oceanic Technology*, *22*, 583–591. https://doi.org/10.1175/jtech1731.1

Simpson, J. H., Bos, W. G., Schirmer, F., Souza, A. J., Rippeth, T. P., Jones, S. E., & Hydes, D. (1993). Periodic stratification in the Rhine ROFI in the North Sea. *Oceanologica Acta*, *16*, 23–32.

Simpson, J. H., & Souza, A. J. (1995). Semidiurnal switching of stratification in the region of the Rhine. *Journal of Geophysical Research*, *100*, 7037–7044. https://doi.org/10.1029/95jc00067

Solodoch, A., Molemaker, J. M., Srinivasan, K., Berta, M., Marie, L., & Jagannathan, A. (2020). Observations of shoaling density current regime changes in internal wave interactions. *Journal of Physical Oceanography*, *50*(6), 1733–1751. https://doi.org/10.1175/JPO-D-19-0176.1

Souza, A. J. (2013). On the use of the Stokes number to explain frictional tidal dynamics and water column structure in shelf seas. *Ocean Science*, *9*, 391–398. https://doi.org/10.5194/os-9-391-2013

Stashchuk, N., & Vlasenko, V. (2009). Generation of internal waves by a supercritical stratified plume. *Journal of Geophysical Research: Oceans*, *114*, 1–17. https://doi.org/10.1029/2008jc004851

Stelling, G. S., & Van Kester, J. A. M. (1994). On the approximation of horizontal gradients in sigma coordinates for bathymetry with steep bottom slopes. *International Journal for Numerical Methods in Fluids*, *18*, 915–935. https://doi.org/10.1002/fld.1650181003

Suijlen, J., & Duin, R. D. (2002). *Atlas of near-surface total suspended matter concentrations in the Dutch coastal zone of the North Sea (Tech. Rep. No. December)*. National Institute for Coastal and Marine Management.

van Alphen, J., De Ruijter, W. P. M., & Borst, J. C. (1988). Outflow and three-dimensional spreading of Rhine river water in the Netherlands coastal zone. In J. Dronkers, & W. van Leussen (Eds.), *Physical processes in estuaries* (pp. 70–92). Springer-Verlag. https://doi.org/10.1007/978-3-642-73691-9_5

Winant, C. D. (2007). Three-dimensional tidal flow in an elongated, rotating basin. *Journal of Physical Oceanography*, *37*, 2345–2362. https://doi.org/10.1175/jpo3122.1

Xie, X., Li, M., & Boicourt, W. C. (2017). Breaking of internal solitary waves generated by an estuarine gravity current. *Geophysical Research Letters*, *44*, 7366–7373. https://doi.org/10.1002/2017gl073824